Hydrothermal combined with electrodeposition construction of stable Co_9S_8/Ni_3S_2@NiFe-LDH heterostructure electrocatalyst for overall water splitting

Fu Liu, Xingzhong Guo*, Yang Hou, Fan Wang, Chang Zou, Hui Yang

Node S1: The characterization of CoMo and Ni_3S_2/NF.

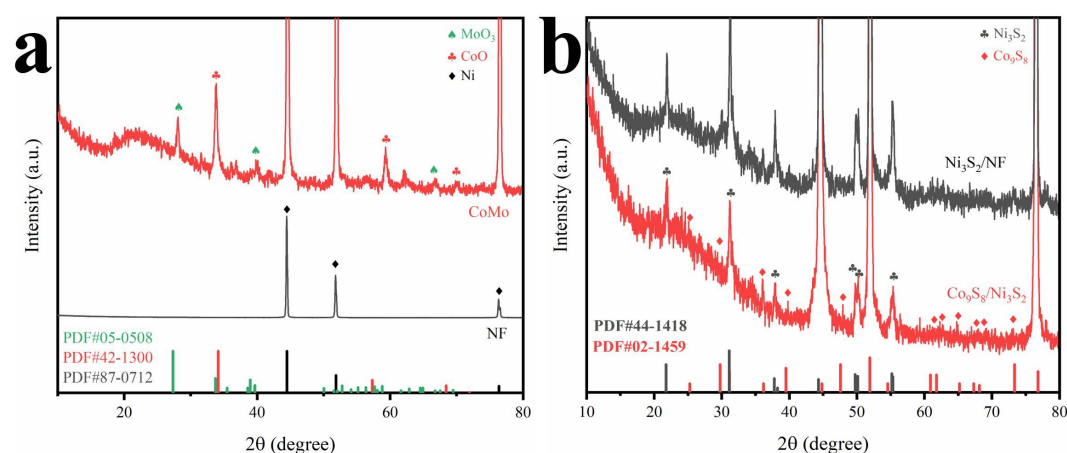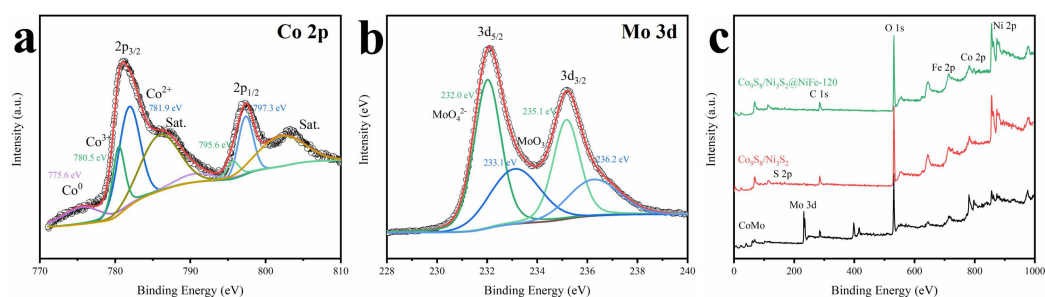**Figure S1.** XRD patterns of the obtained samples: (a) nickel foam and CoMo,(b) Ni_3S_2/NF and Co_9S_8/Ni_3S_2.

Figure S2. (a) Co 2p, (b) Mo 3d high resolution XPS spectra for CoMo, (c) The entire XPS spectra of CoMo, Co_9S_8/Ni_3S_2, Co_9S_8/Ni_3S_2@NiFe-120.

Figure S2a shows the Co 2p spectrum, in which the peaks at 780.5 eV and 795.6 eV are attributed to $2p_{3/2}$ and $2p_{1/2}$ of Co^{3+}, the peaks at 781.9 eV and 797.3 eV are attributed to $2p_{3/2}$ and $2p_{1/2}$ of Co^{2+} in cobalt oxides, respectively. Besides, the Co^{3+}/ Co^{2+} molar ratio is 0.45:1, and the peak at 775.6 eV indicates the existence of Co^0. For Mo 3d spectrum (Figure S2b), the $3d_{5/2}$ and $3d_{3/2}$ locate at 232.0 eV and 235.1 eV are assigned to Mo in MoO_4^{2-} which combined with Co to form $CoMoO_4$ [1], and 233.1 eV and 236.2 eV are assigned to MoO_3 [2]. The above results are in agreement with XRD results (Figure S1a), confirming the formation of CoO and MoO_3
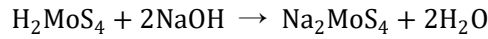
1

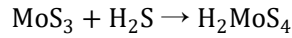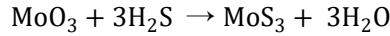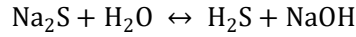compounds. In the entire spectra of CoMo, Co_9S_8/Ni_3S_2 and Co_9S_8/Ni_3S_2@NiFe-120 (Figure S2c), it's easy to observe that Mo disappears in Co_9S_8/Ni_3S_2 and Co_9S_8/Ni_3S_2@NiFe-120, which also coincides with the XRD results (Figure S2b).

Node S2: The explanation and certification of the disappearance of Mo.

**Table S1.** Metal elements concentration detected by ICP-MS analysis.

| Samples	Co (mg·L^{-1})	Mo (mg·L^{-1})	Na (mg·L^{-1})
CoMo	392.22	398.26	0.991
Co$_9$S$_8$/Ni$_3$S$_2$	195.76	0.95	0.993
Solution	0.0125	240.76	2884.91

The original ICP-MS results are shown in Table S1, in which we only detect the content of Co, Mo and Na. For CoMo, the content ratio of Co and Mo is about 1:1, while Na is considered as an impurity element reserved from Na$_2$MoO$_4$·2H$_2$O or Na$_2$S during the preparation. However, after the sulfuration, the content ratio of Co and Mo comes to almost 200:1, the concentration of Mo is near to that of Na, indicating that Mo was wiped off during the sulfuration. Furtherly, we also measured the ion concentration of the solution, in which the content of Mo greatly exceeded Co, proving that Mo almost distributed in solution. Besides, Na was from Na$_2$S, thus possessed a high concentration. The possible reactions for Mo during the sulfuration are shown as follows:

$$Na_2S + H_2O \leftrightarrow H_2S + NaOH$$

$$MoO_3 + 3H_2S \rightarrow MoS_3 + 3H_2O$$

$$MoS_3 + H_2S \rightarrow H_2MoS_4$$

$$H_2MoS_4 + 2NaOH \rightarrow Na_2MoS_4 + 2H_2O$$

When Na$_2$S is excessive, the generated MoS$_3$ can furtherly react with H$_2$S during the hydrothermal process and finally dissolve in H$_2$O in the form of Na$_2$MoS$_4$, resulting in the disappearance of Mo in samples. To certify the above reactions, we dropped 1 M hydrochloric acid (HCl) into the solution after sulfuration, based on the following reactions:

$$Na_2MoS_4 + 2HCl \rightarrow H_2MoS_4 + 2NaCl$$

$$H_2MoS_4 \rightarrow MoS_3 + H_2S$$
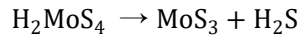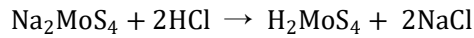
After the addition of HCl, an odor of H$_2$S could be smelled, which might come from the excessive Na$_2$S and the resultant H$_2$MoS$_4$, and brown sediments also appeared, as shown in Figure S3a. The sediments were washed and treated in Ar at 700 °C to remove sulfur in MoS$_3$ to form crystalline MoS$_2$ in the following reaction:

$$MoS_3 \xrightarrow{700\,°C} MoS_2 + S$$
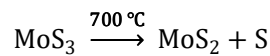
The XRD pattern shows the composition of the sediments before and after heat treatment in Figure S3b, c, respectively. The XRD pattern of sediments shows no obvious diffraction peaks, suggesting the amorphous phase, while after heat treatment, the sediments have peaks

corresponding to MoS$_2$ (PDF#37-1492), proving the formation of MoS$_3$ in sediments. The results prove the above discussion and explain the disappearance of Mo in samples.
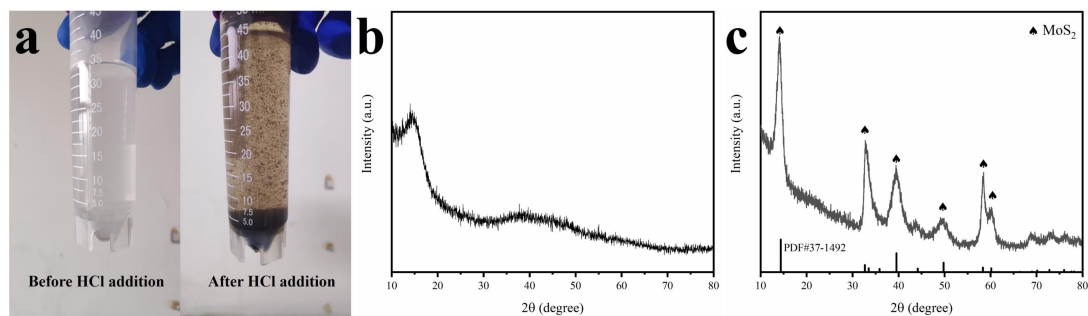

Figure S3. (a) Pictures of the solution obtained in hydrothermal procedure before and after HCl addition, XRD patterns of (b) sediments, (c) sediments after 700 ℃ heat treatment in Ar.

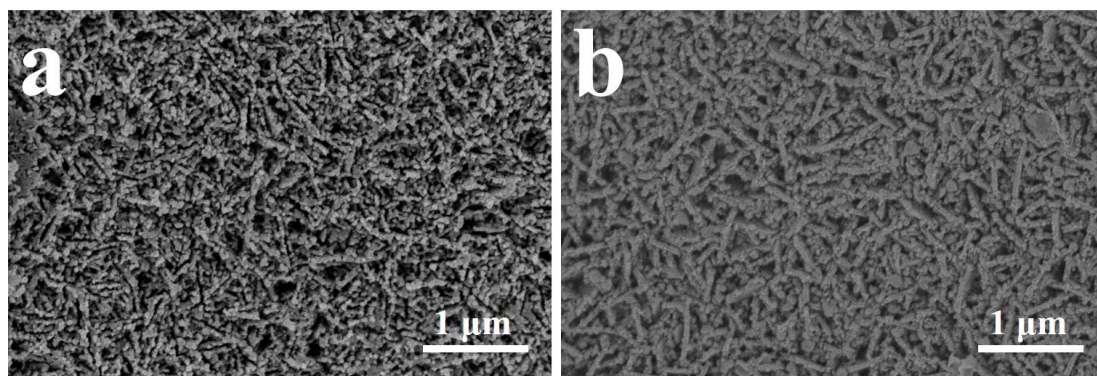

Figure S4. FESEM images of samples with different Na$_2$S dosage in hydrothermal procedure: (a) 0.023 g, (b) 0.005 g
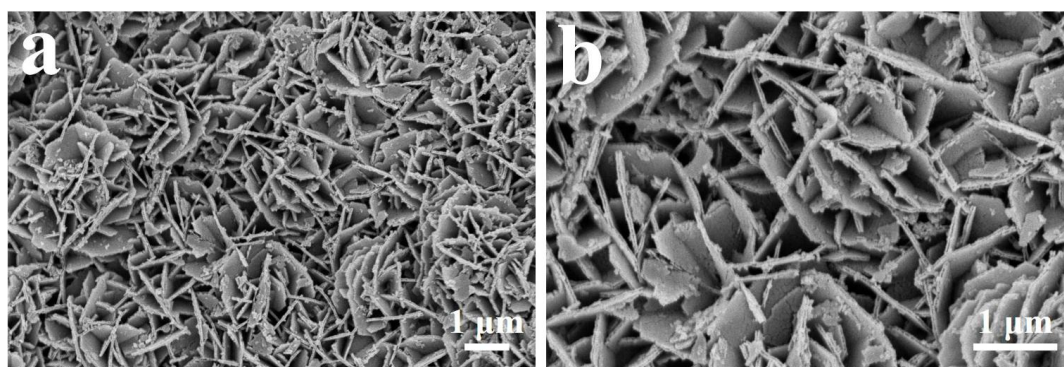

Figure S5. FESEM images of the sample with 0.234 g Na$_2$S dosage in hydrothermal procedure for 1 h
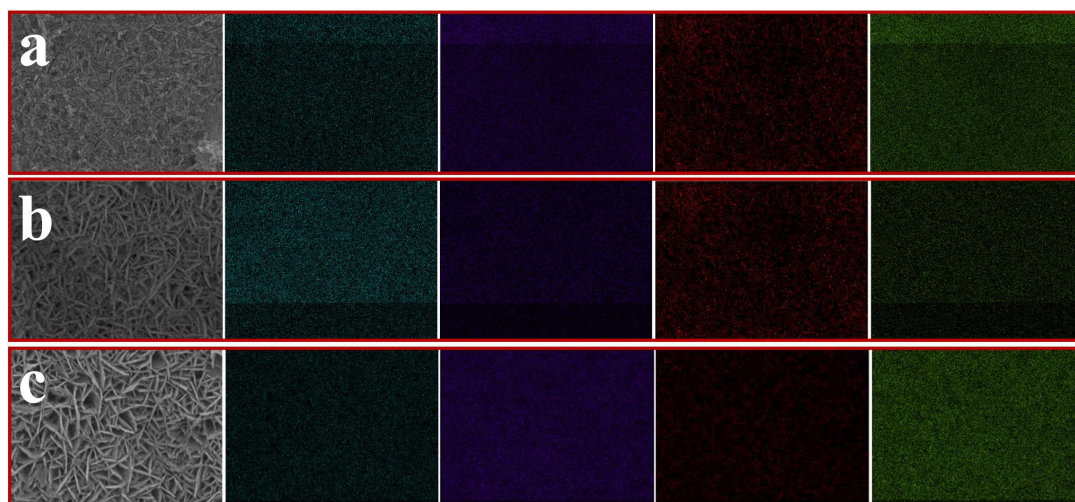
Figure S6. FESEM images and corresponding element mapping of different samples: (a) 0.023 g Na$_2$S dosage for 6h, (b) 0.005 g Na$_2$S dosage for 6h, (c) 0.234 g Na$_2$S dosage for 1h with the same Na$_2$S dosage in hydrothermal procedure for 1 h

Table S2. The element ratio of different samples after sulfuration obtained by EDS.

Sample	Co (at%)	Mo (at%)	O (at%)	S (at%)
Sample wth 0.023 g Na$_2$S dosage for 6h	15.19	8.38	47.88	28.55
Sample wth 0.005 g Na$_2$S dosage for 6h	12.20	10.42	75.04	2.34
Sample wth 0.234 g Na$_2$S dosage for 1h	18.46	1.72	35.47	44.35

We furtherly conduct the sulfuration procedure using less Na$_2$S dosage, the FESEM images are shown in Figure S4. It indicates that little Na$_2$S can only react on the surface of CoMo nanosheets and is not able to change the spatial arrangement. Another sample with the same Na$_2$S dosage for 1 h hydrothermal procedure was also prepared and the FESEM images are shown in Figure S5, it's obvious that larger sheet size and space are obtained. The element distribution and ratio of the three samples obtained by EDS are shown in Figure S6 and Table S2, further confirming the effect of excessive Na$_2$S dosage.
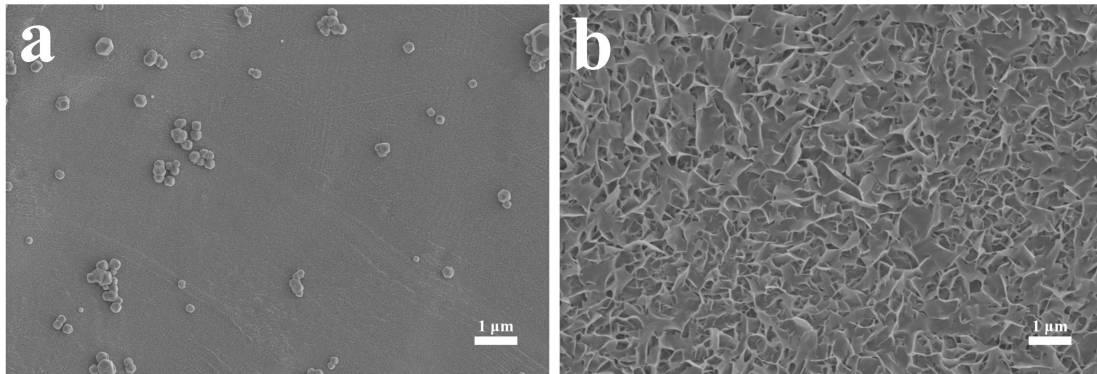
Figure S7. FESEM images of samples prepared using the same hydrothermal condition with only one precursor: (a) $Co(NO_3)_2·6H_2O$, (b) $Na_2MoO_4·2H_2O$.

As shown in Figure S5, merely using one raw material ($Co(NO_3)_2·6H_2O$ or $Na_2MoO_4·2H_2O$) cannot obtain the large-size sheets which can be used as substrates in electrodeposition.

Therefore, there was a recomposition during the sulfuration process, resulting in larger sizes of nanosheets, moreover, benefiting from the reactions between MoO_3 and Na_2S, the interspace of nanosheets became larger, the larger sizes and interspace were both beneficial to electrodeposition. In previous reports, the obtained Co_9S_8 is often small sheets, such as Zhou *et al* [3], Du *et al* [4] or nanowires, such as Du *et al* [5], thus this may be an effective method to prepare large-size sulfides.

Node S3: The characterizations of Co$_9$S$_8$/Ni$_3$S$_2$, Co$_9$S$_8$/Ni$_3$S$_2$@NiFe-60, Co$_9$S$_8$/Ni$_3$S$_2$@NiFe-120 and Co$_9$S$_8$/Ni$_3$S$_2$@NiFe-180.

Table S3. Metal element concentration detected by ICP-MS analysis for the solution with different element concentrations in electrodeposition.

Ni/Fe ratio in solution	Ni (mg·L^{-1})	Fe (mg·L^{-1})	Ni (mol·L^{-1})	Fe (mol·L^{-1})
1:1	5.688	7.512	0.0969	0.1345
1:2	2.203	5.011	0.0375	0.0897
2:1	6.795	5.171	0.1158	0.0926

The pK_{sp} of Ni^{2+} is 15.26, while the pK_{sp} of Fe^{2+} is 16.31, indicating that Fe^{2+} is more liable to deposit during the electrodeposition procedure.
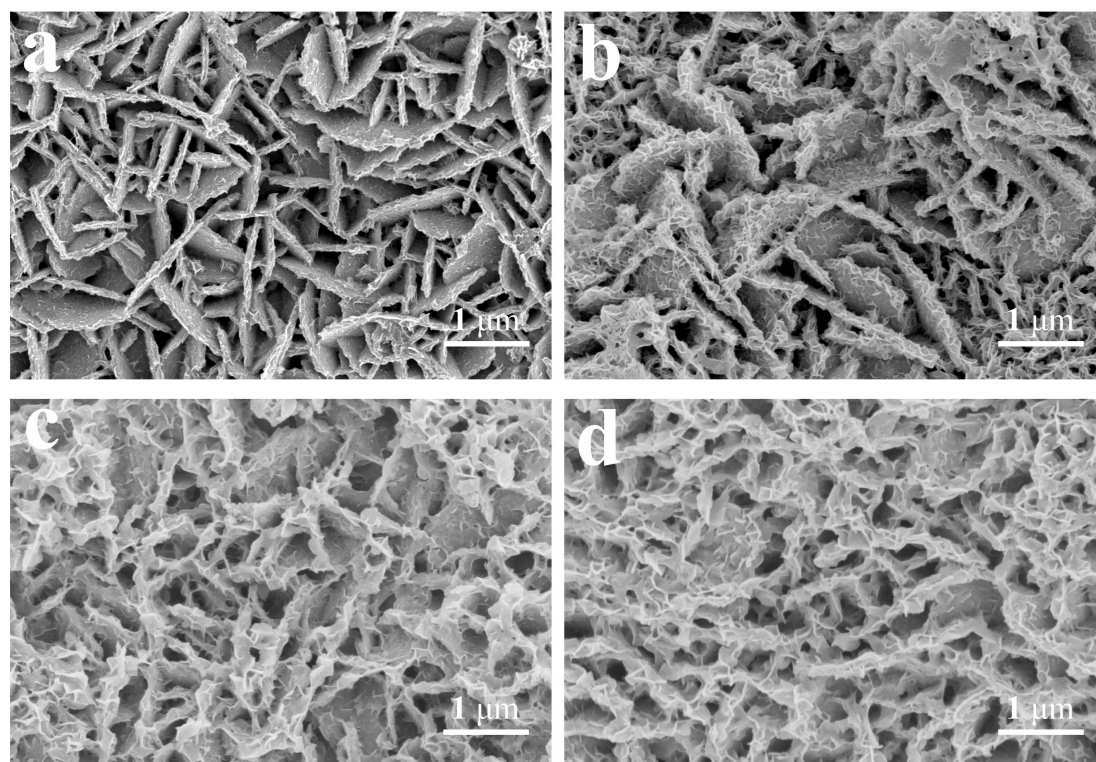

Figure S8. FESEM images of (a) Co$_9$S$_8$/Ni$_3$S$_2$, (b) Co$_9$S$_8$/Ni$_3$S$_2$@NiFe-60, (c) Co$_9$S$_8$/Ni$_3$S$_2$@NiFe-120, (d) Co$_9$S$_8$/Ni$_3$S$_2$@NiFe-180.
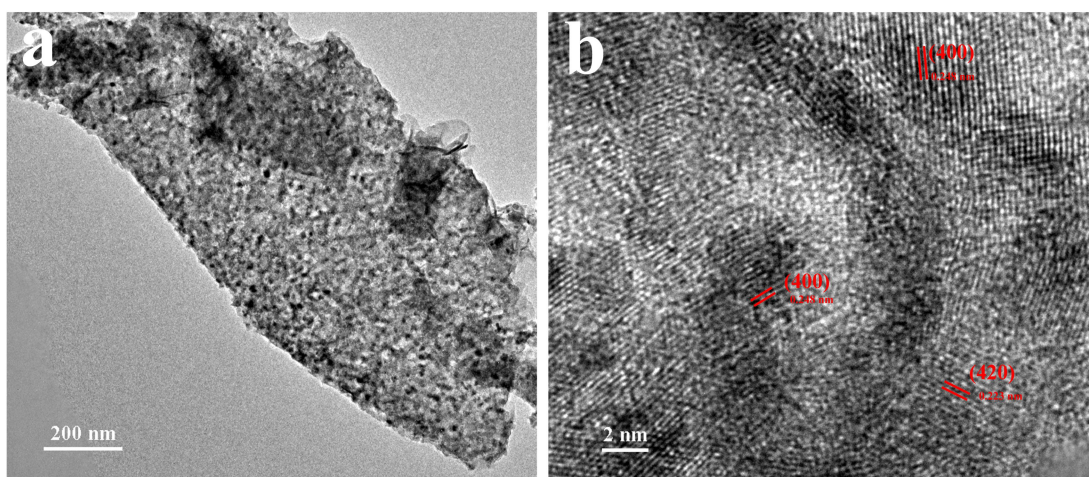
Figure S9. TEM images of Co$_9$S$_8$/Ni$_3$S$_2$ sample: (a) Co$_9$S$_8$ nanosheet, (b) high-resolution image of Co$_9$S$_8$ nanosheet.
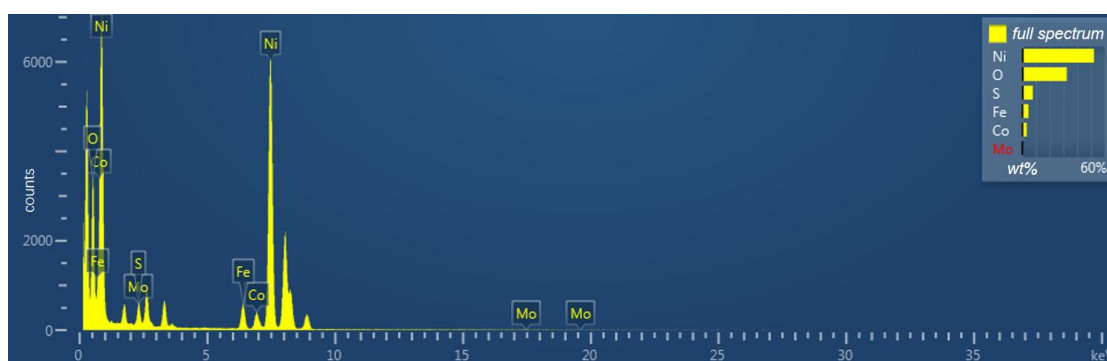
Figure S10. EDX spectrum and atomic mass distribution of Co$_9$S$_8$/Ni$_3$S$_2$@NiFe-120.
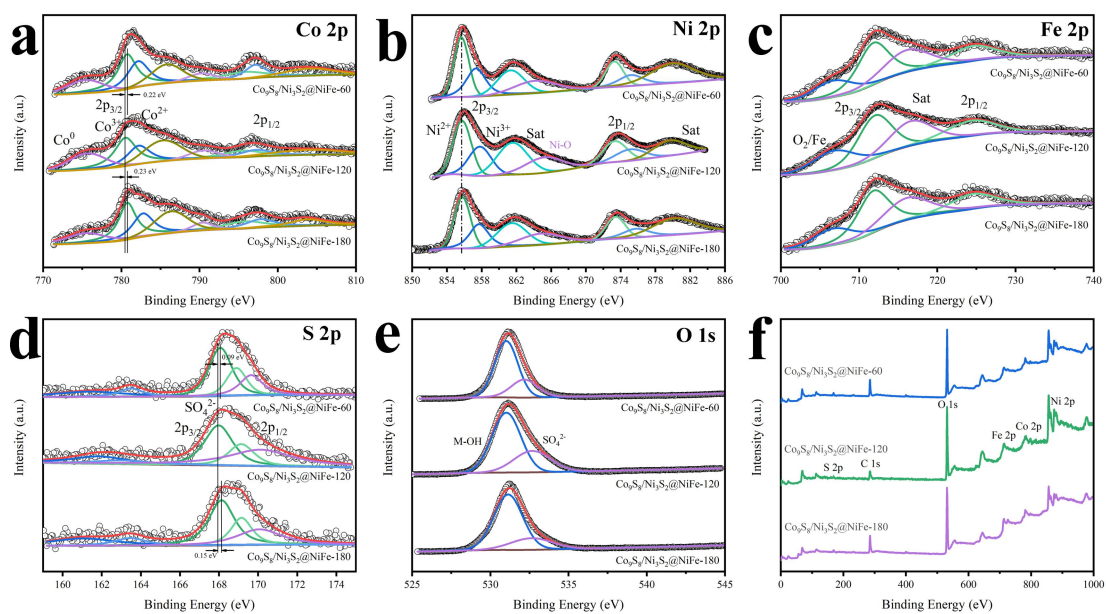
Figure S11. XPS spectra of Co$_9$S$_8$/Ni$_3$S$_2$@NiFe-60, Co$_9$S$_8$/Ni$_3$S$_2$@NiFe-120 and Co$_9$S$_8$/Ni$_3$S$_2$@NiFe-180: (a) Co 2p, (b) Ni 2p, (c) Fe 2p, (d) S 2p, (e) O 1s, (f) entire region.

Node S4: The measurements and characterizations of catalysts for water splitting.
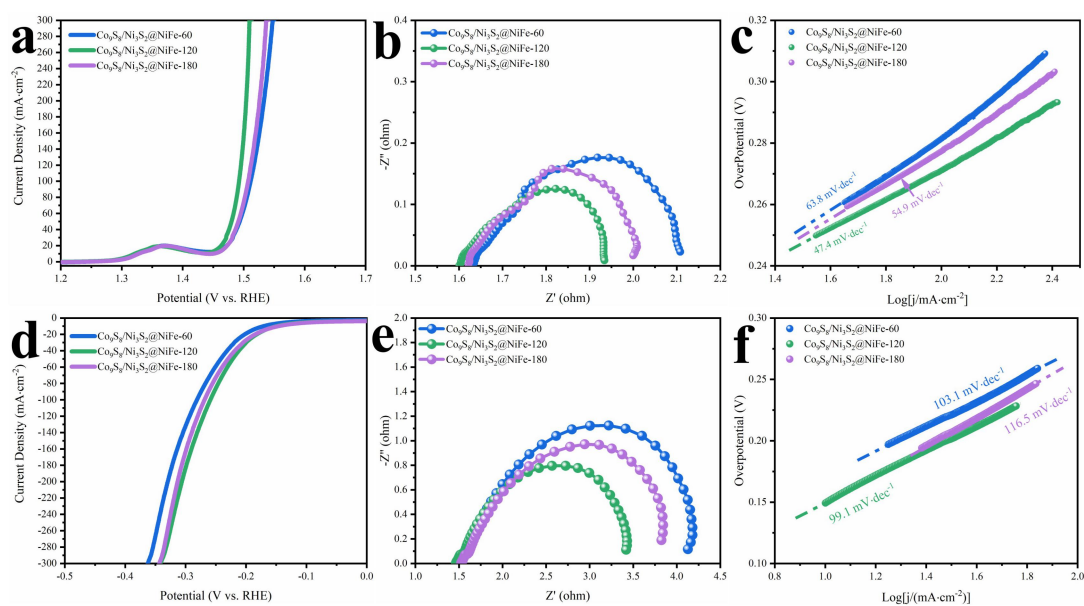
Figure S12. The electrocatalytic performance comparison of $Co_9S_8/Ni_3S_2@NiFe$-60, $Co_9S_8/Ni_3S_2@NiFe$-120 and $Co_9S_8/Ni_3S_2@NiFe$-180, (a) LSV, (b) EIS, (c) Tafel plots for OER and (d) LSV, (e) EIS, (f) Tafel plots for HER.
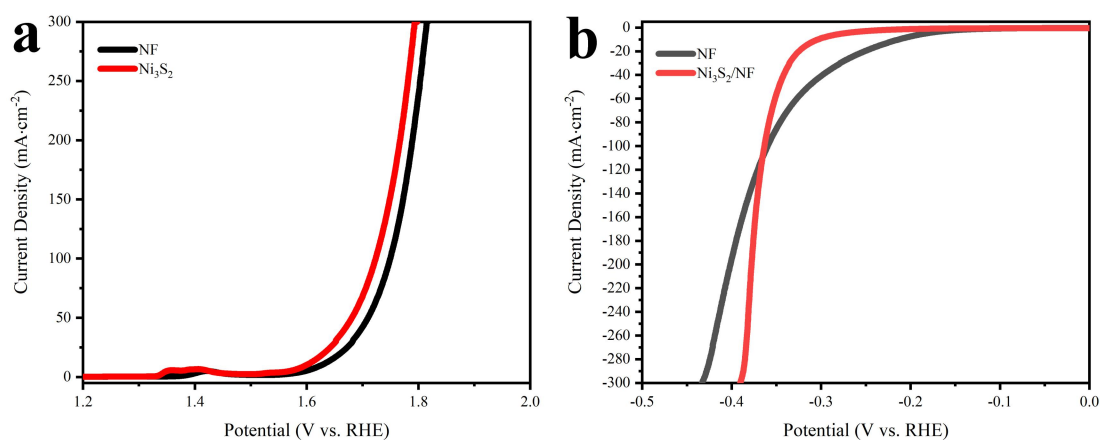
Figure S13. LSV curves of NF and Ni_3S_2/NF for (a) OER and (b) HER.
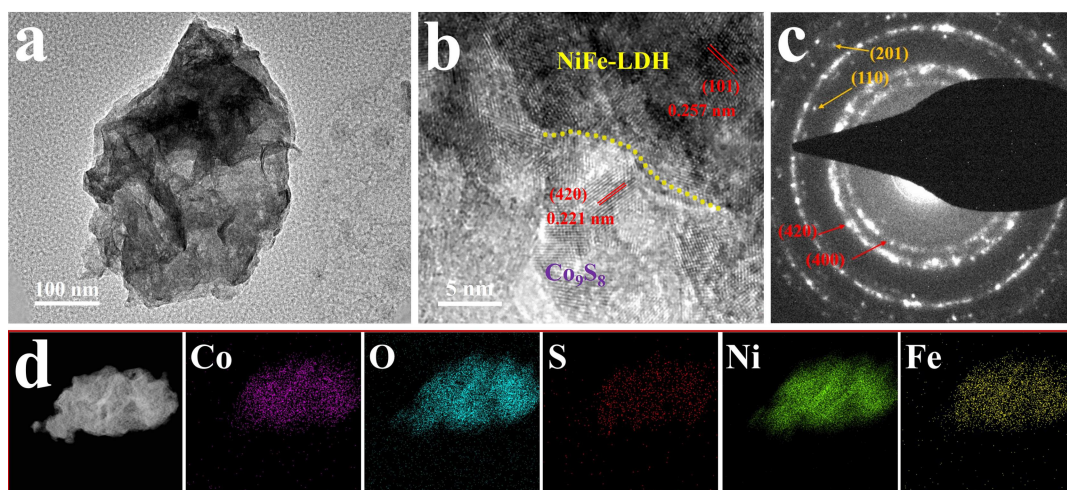
Figure S14. (a) TEM, (b) HRTEM, (c) selected area electron diffraction (SAED) images and (d) corresponding element mappings of Co_9S_8/Ni_3S_2@NiFe-120 after long term OER test.
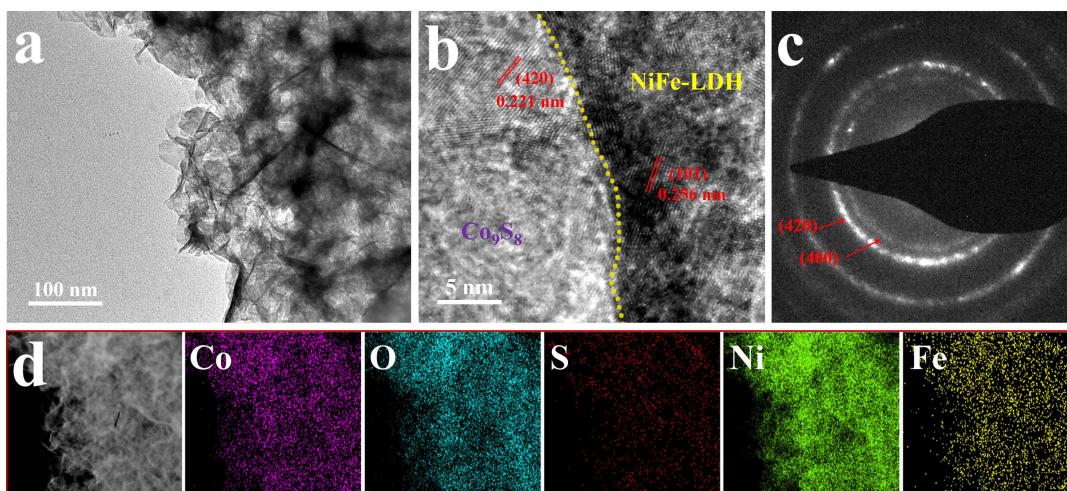
Figure S15. (a) TEM, (b) HRTEM, (c) selected area electron diffraction (SAED) images and (d) corresponding element mappings of Co_9S_8/Ni_3S_2@NiFe-120 after long term HER test.
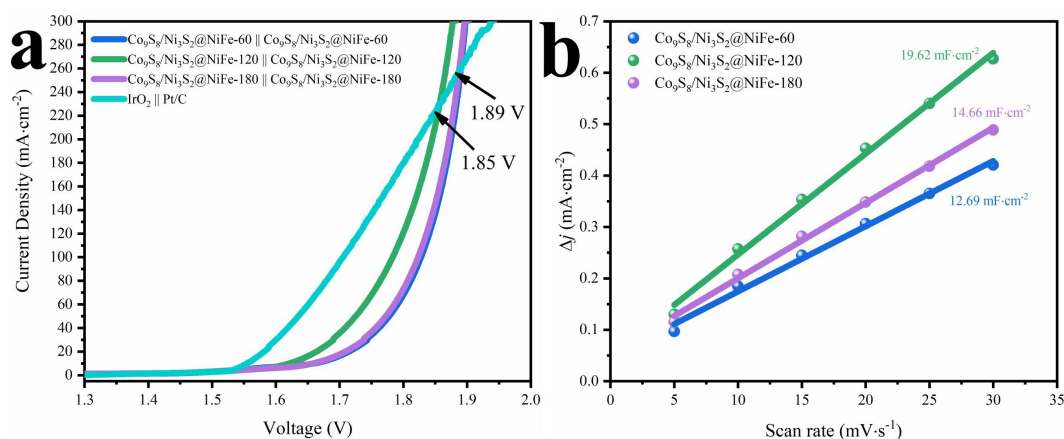
Figure S16. The electrocatalytic performance comparison of Co_9S_8/Ni_3S_2@NiFe-60, Co_9S_8/Ni_3S_2@NiFe-120 and Co_9S_8/Ni_3S_2@NiFe-120, (a) LSV, (b) Capacitive current densities as a function of various scan rates for the three catalysts.

Table S4. Comparison of serval similar electrocatalysts for OER.

| Electrocatalyst	Overpotential (mV) at 10 mA·cm^{-2}	Overpotential (mV) at 100 mA·cm^{-2}	Tafel slope (mV·dec^{-1})	Reference
$Co_9S_8/Ni_3S_2@NiFe$-120	229	262	47.4	This work
Ni_3S_2/Co_9S_8	/	340	66	6
$Co_{1.8}Ni(OH)_{5.6}@Co_{1.8}NiS_{0.4}(OH)_{4.8}$	274	/	45.0	7
$Cu@CoP$	270	≈350	77.2	8
Co_9S_8/Ni_3S_2	227	≈280	46.5	5
CCS Ni-Co Nw	302	≈310	43.6	9
$Co_3S_4@MoS_2$	280	≈320	43	10
CoMoNiS-NF-31	166	350	58	11
MoS_2/Ni_3S_2	218	290	88	12
$(Ni,Fe)S_2@MoS_2$	270	320	43.21	13
Co1Mn1CH/NF	/	349	/	14
Co_9S_8/Co_3O_4	250	/	73.54	15
$NiS_{0.5}Se_{0.5}$	257	320	61	16

Table S5. The charge transfer resistance (R_{ct}) based on the Nyquist plots for OER.

Samples	R_{ct} (Ω·cm^{-2})
CoMo	1.91
Co_9S_8/Ni_3S_2	0.95
NiFe-120/NF	0.45
$Co_9S_8/Ni_3S_2@NiFe$-60	0.51
$Co_9S_8/Ni_3S_2@NiFe$-120	0.32
$Co_9S_8/Ni_3S_2@NiFe$-180	0.48

Table S6. Comparison of serval similar electrocatalysts for HER.

Electrocatalyst	Overpotential (mV) at 10 mA·cm^{-2}	Overpotential (mV) at 100 mA·cm^{-2}	Tafel slope (mV·dec^{-1})	Reference
Co_9S_8/Ni_3S_2@NiFe-120	151	259	99.1	This work
Ni_3S_2/Co_9S_8	/	269	98	6
Cu@CoP	88	150	66.1	8
Co_9S_8/Ni_3S_2	128	≈230	97.6	5
Co_3S_4@MoS_2	136	/	74	10
CoMoNiS-NF-31	113	/	85	11
MoS_2/Ni_3S_2	110	/	83.1	12
(Ni, Fe)S_2@MoS_2	130	240	101.22	13
Co1Mn1CH/NF	180	328	/	14
$NiS_{0.5}Se_{0.5}$	70	105	78	16
Cu_xS@NiCo-LDH	107	≈190	/	17
$Ni(OH)_2$/MoS_2	80	155	60	18

Table S7. The charge transfer resistance (R_{ct}) based on the Nyquist plots for HER.

Samples	R_{ct} (Ω·cm^{-2})
CoMo	8.45
Co_9S_8/Ni_3S_2	4.05
NiFe-120/NF	13.63
Co_9S_8/Ni_3S_2@NiFe-60	2.67
Co_9S_8/Ni_3S_2@NiFe-120	1.96
Co_9S_8/Ni_3S_2@NiFe-180	2.31

Table S8. Comparison of serval similar electrocatalysts for overall water splitting cell.

Electrocatalyst	Cell voltage (V) at 10 mA·cm^{-2}	Reference
Co_9S_8/Ni_3S_2@NiFe-120	1.62	This work
Ni_3S_2/Co_9S_8	1.55	6
Cu@CoP	1.65	8
Co_9S_8/Ni_3S_2	1.64	5
Co_3S_4@MoS_2	1.58	10
CoMoNiS-NF-31	1.54	11

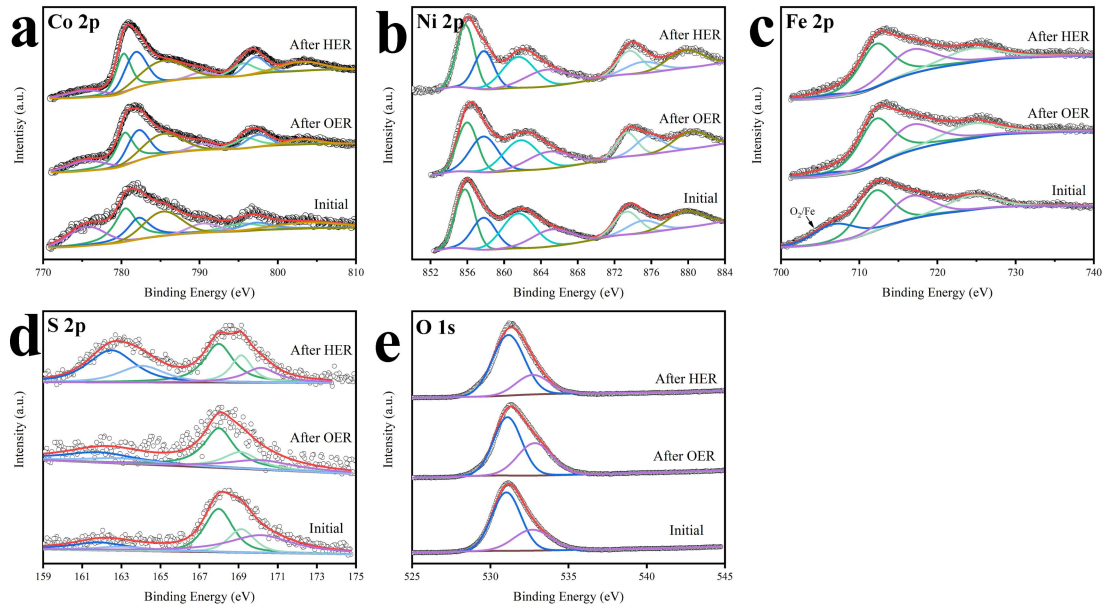|		
MoS$_2$/Ni$_3$S$_2$	1.56	12
NiS$_{0.5}$Se$_{0.5}$	1.55	16

Figure S17. XPS spectra of Co$_9$S$_8$/Ni$_3$S$_2$@NiFe-120 after 24 h durability tests for OER and HER: (a) Co 2p, (b) Ni 2p, (c) Fe 2p, (d) S 2p, (e) O 1s region.

For Co, after the water splitting reaction, the ratio of high spin Co^{3+} increased and Co^0 reduced, which is beneficial to the charge transfer process [19], indicating the optimization of electron structure of Co$_9$S$_8$ nanosheets core during the reactions, the Co-O belongs to the intermediate reactant of OER and HER results to the rising valance state, proving the oxidation of Co$_9$S$_8$. For Fe, the peak at 706.7 eV which represents O$_2$/Fe derived from the adsorbed oxygen in air reduced after the reactions, indicating that NiFe-LDHs contributed to the reaction process. Besides, the S-O peaks present strong intensity after HER, corresponding to the S-OH during the reaction.
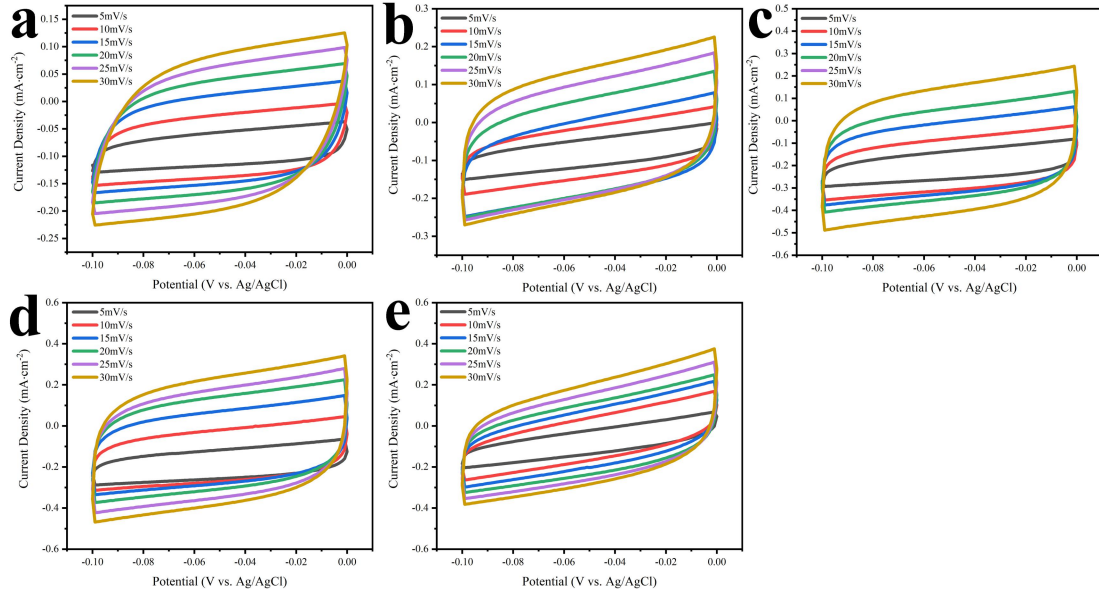
Figure S18. CV curves of (a) CoMo, (b) Co_9S_8/Ni_3S_2, (c) $Co_9S_8/Ni_3S_2@NiFe-60$, (d) $Co_9S_8/Ni_3S_2@NiFe-120$, (e) $Co_9S_8/Ni_3S_2@NiFe-180$ at different scan rates (5, 10, 15, 20, 25, 30 $mV \cdot s^{-1}$) in the non-faradic potential of -0.1~0 V vs. Ag/AgCl.
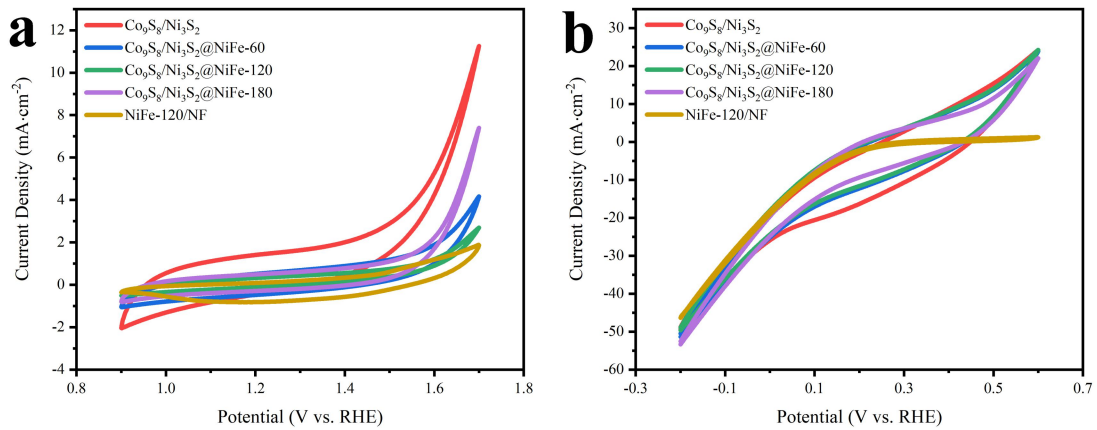
Figure S19. CV curves of Co_9S_8/Ni_3S_2, $Co_9S_8/Ni_3S_2@NiFe-60$, $Co_9S_8/Ni_3S_2@NiFe-120$, $Co_9S_8/Ni_3S_2@NiFe-180$ and NiFe-120/NF at a scan rate of 50 mV·s-1 in 1.0 M PBS (pH=7) for (a) OER and (b) HER.

In Figure S19, turnover frequency (TOF) was estimated to investigate the intrinsic catalytic activity of the catalysts，its value can be calculated by the equations: TOF = $(jA)/(4nF)$ for OER and TOF = $(jA)/(2nF)$ for HER, j is the current density at a constant overpotential, A is the area of the working electrode and F is Faraday's constant (96485 C·mol^{-1}) [20], n is the number of active sites which can be calculated by the equation: $n = Q/4F$ for OER and $n = Q/2F$ for HER, where Q is the integral charges obtained by CV tests at 0.9 ~ 1.7 (-0.2 ~ 0.6) V vs. RHE for OER (HER) in a phosphate buffer solution (pH=7.0) [21]

14

Table S9. TOF values of Co_9S_8/Ni_3S_2, $Co_9S_8/Ni_3S_2@NiFe-60$, $Co_9S_8/Ni_3S_2@NiFe-120$, $Co_9S_8/Ni_3S_2@NiFe-180$ and NiFe-120/NF at an overpotential of 200 mV.

TOF(s^{-1})	Co_9S_8/Ni_3S_2	$Co_9S_8/Ni_3S_2@$ NiFe-60	$Co_9S_8/Ni_3S_2@$ NiFe-120	$Co_9S_8/Ni_3S_2@$ NiFe-180	NiFe-120/NF
OER	0.124	0.708	1.353	0.465	0.169
HER	0.054	0.065	0.111	0.101	0.110

The Faradic Efficiency was also estimated using the equation: $FE=V_{exp}/V_{cal}=n_{exp}/n_{cal}$, in which V_{exp} and V_{cal} are the experimental and calculated gas volume (O_2 or H_2) during the reaction, respectively, n_{exp} and n_{cal} are the experimental and calculated gas quantity. n_{exp} and n_{cal} can be calculated using the following equations [22, 23]:

$$n_{exp} = C_1 n_{gas}$$

C_1: concentration of gas products (mol·mol^{-1})

n_{gas}: amount of gas injected to gas chromatography (GC), calculated by $n_{gas} = PV_o/RT$, $V_o = 1$ mL (volume of gas sample), $P = 1.013 \times 10^5$ Pa, $R = 8.314$ N·m·K^{-1}, $T = 293.15$ K

$$n_{cal} = \frac{jt}{ZF}$$

j: the steady-state current, here we choose 50 mA as the testing current

t: reaction time

Z: the number of electrons required to generate on molecule of gas, for H_2, $Z = 2$, and for O_2, $Z = 4$.

F: Faraday's constant (96485 C·mol^{-1})

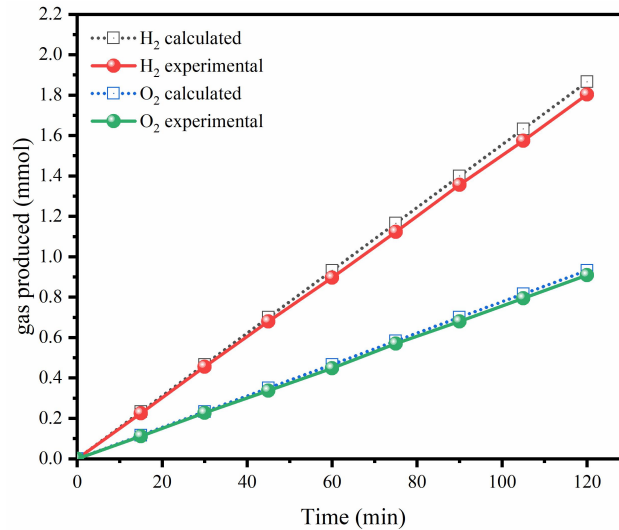The results are shown in **Figure** S15.

Figure S20. The quantity of gas theoretically calculated and experimentally measured versus time employing $Co_9S_8/Ni_3S_2@NiFe-120$ catalysts as both anode and cathode at current density of 50 mA· cm^{-2}.

References:

1 W. Wang, T. Wang, X. Fan, C. Zhang, J. Hu, H. Chen, Z. Fang, J. Yan and B. Liu, *Chemical Research in Chinese Universities*, 2019, **35**, 261-270.

2 K. Li, J. Ma, X. Guan, H. He, M. Wang, G. Zhang, F. Zhang, X. Fan, W. Peng and Y. Li, *Nanoscale*, 2018, **10**, 22173-22179.

3 Y. Zhou, J. Zhang, F. Sun, X. Yu, W. Kang and J. Zhang, *Journal of Solid State Chemistry*, 2020, **285**, 121230.

4 X. Du, H. Su and X. Zhang, *Journal of Alloys and Compounds*, 2020, **824**, 153965.

5 F. Du, L. Shi, Y. Zhang, T. Li, J. Wang, G. Wen, A. Alsaedi, T. Hayat, Y. Zhou and Z. Zou, *Applied Catalysis B: Environmental*, 2019, **253**, 246-252.

6 J. Lin, H. Wang, X. Zheng, Y. Du, C. Zhao, J. Qi, J. Cao, W. Fei and J. Feng, *Journal of Power Sources*, 2018, **401**, 329-335.

7 B. Wang, C. Tang, H. F. Wang, X. Chen, R. Cao and Q. Zhang, *Adv Mater*, 2019, **31**, e1805658.

8 P. Wang, Y. Lin, L. Wan and B. Wang, *Energy & Fuels*, 2020, **34**, 10276-10281.

9 S.-H. Bae, J.-E. Kim, H. Randriamahazaka, S.-Y. Moon, J.-Y. Park and I.-K. Oh, *Advanced Energy Materials*, 2017, **7**, 1601492.

10 Y. Guo, J. Tang, Z. Wang, Y.-M. Kang, Y. Bando and Y. Yamauchi, *Nano Energy*, 2018, **47**, 494-502.

11 Y. Yang, H. Yao, Z. Yu, S. M. Islam, H. He, M. Yuan, Y. Yue, K. Xu, W. Hao, G. Sun, H. Li, S. Ma, P. Zapol and M. G. Kanatzidis, *Journal of the American Chemical Society*, 2019, **141**, 10417-10430.

12 J. Zhang, T. Wang, D. Pohl, B. Rellinghaus, R. Dong, S. Liu, X. Zhuang and X. Feng, *Angewandte Chemie International Edition*, 2016, **55**, 6702-6707.

13 Y. Liu, S. Jiang, S. Li, L. Zhou, Z. Li, J. Li and M. Shao, *Applied Catalysis B: Environmental*, 2019, **247**, 107-114.

14 T. Tang, W.-J. Jiang, S. Niu, N. Liu, H. Luo, Y.-Y. Chen, S.-F. Jin, F. Gao, L.-J. Wan and J.-S. Hu, *Journal of the American Chemical Society*, 2017, **139**, 8320-8328.

15 D. Peng, B. Zhang, J. Wu, K. Huang, X. Cao, Y. Lu, Y. Zhang, C. Li and Y. Huang, *ChemCatChem*, 2020, **12**, 2431-2435.

16 Y. Wang, X. Li, M. Zhang, Y. Zhou, D. Rao, C. Zhong, J. Zhang, X. Han, W. Hu, Y. Zhang, K. Zaghib, Y. Wang and Y. Deng, *Advanced Materials*, 2020, DOI: 10.1002/adma.202000231, 2000231.

17 X. Deng, X. Kang, M. Li, K. Xiang, C. Wang, Z. Guo, J. Zhang, X.-Z. Fu and J.-L. Luo, *Journal of Materials Chemistry A*, 2020, **8**, 1138-1146.

18 B. Zhang, J. Liu, J. Wang, Y. Ruan, X. Ji, K. Xu, C. Chen, H. Wan, L. Miao and J. Jiang, *Nano Energy*, 2017, **37**, 74-80.

19 F. Si, C. Tang, Q. Gao, F. Peng, S. Zhang, Y. Fang and S. Yang, *Journal of Materials Chemistry A*, 2020, **8**, 3083-3096.

20 R. Yang, Y. Zhou, Y. Xing, D. Li, D. Jiang, M. Chen, W. Shi and S. Yuan, *Applied Catalysis B: Environmental*, 2019, **253**, 131-139.

21 H. Liao, X. Guo, Y. Hou, H. Liang, Z. Zhou and H. Yang, *Small*, 2020, **16**, e1905223.

22 F. Wei, T. Wang, X. Jiang, Y. Ai, A. Cui, J. Cui, J. Fu, J. Cheng, L. Lei, Y. Hou and S. Liu, *Advanced Functional Materials*, 2020, **30**, 2002092.

23 Y. Lin, D. Zhang and Y. Gong, *Applied Surface Science*, 2020, DOI: